Continental Shelf Research 291 (2025) 105466

Contents lists available at ScienceDirect

Continental Shelf Research

journal homepage: www.elsevier.com/locate/csr

Research papers

On the wind-driven European shelf sea-level variability and the associated oceanic circulation

Sam T. Diabaté [a,b,c,*], Neil J. Fraser [a], Martin White [d], Barbara Berx [e], Louis Marié [f], Gerard D. McCarthy [c]

[a] The Scottish Association for Marine Science (SAMS), Scottish Marine Institute, Oban, Argyll and Bute, Scotland, UK
[b] Direction des Opérations pour la Prévision, Département Prévision Marine et Océanographie (DirOP/MAR), Météo France, Toulouse, France
[c] The Irish Climate Analysis and Research UnitS (ICARUS), Department of Geography, Maynooth University, Maynooth, Co. Kildare, Republic of Ireland
[d] Earth and Life Sciences, University of Galway, Galway, Republic of Ireland
[e] Marine Directorate, Scottish Government, 375 Victoria Rd, Aberdeen, AB11 9DB, Scotland, UK
[f] Univ. Brest, CNRS, IFREMER, IRD, Laboratoire d'Océanographie Physique et Spatiale (LOPS), IUEM, Plouzané, F-29280, France

ARTICLE INFO

Keywords:
Sea-level changes
Shelf variability
In-situ currents
Wind forcing
Rockall slope current
European slope current
Sub-annual timescales

ABSTRACT

The shelf to the west of Ireland, France and the United Kingdom is a region where currents and sea level respond to the wind activity in a remarkable manner throughout a range of timescales. Using altimetry-obtained measurements and a wind reanalysis, we demonstrate in the present contribution how the sub-annual sea-level variability can be understood as a response to the wind action. The winds drive water towards (away from) the coastline through Ekman transport, yielding sea-level changes coherent along and across the shelf and with maximum amplitude at the coast. The alignment of the winds with the isobaths determines the magnitude of sea-level changes. To investigate the impacts of these changes on the circulation variability, we bring together a comprehensive dataset of 30+ in-situ observations of recent current changes. Using these measurements, we show that sub-annual changes in the shelf-edge circulation from the Goban Spur to the Faroe-Shetland Channel arise from the geostrophic adjustment to shelf sea-level variations induced by the Ekman-driven accumulation of water towards the coastline. Our analysis suggests that the along-isobath current generated through this mechanism are primarily found over the shelf, only *impinge* on the upper slope, and do not affect the circulation above greater depth (>500 m). Nonetheless, important slope circulations such as the Rockall Slope Current are substantially influenced on their shoreward side by this simple geostrophic adjustment process. Because sea-level changes co-vary over large distances on the shelf, there also is remarkable along-isobath coherence in the associated current changes but we warn against concluding this is evidence for the continuity of an 'European Slope Current' circumnavigating the European slope from Portugal to Norway.

1. Introduction

Above and around the continental shelf to the west of France, Ireland, and the United Kingdom (UK), the forcing action of atmospheric variability is well known to affect oceanic currents and sea level (Chafik et al., 2017; Pingree et al., 1999; Gordon and Huthnance, 1987; Le Boyer et al., 2013; Plag and Tsimplis, 1999; Chafik et al., 2019; Calafat et al., 2012). In particular, wind stress exerts an important control on shelf and slope dynamics throughout a range of timescales, from those associated to localised storms (Gordon and Huthnance, 1987) to those associated with large-scale atmospheric modes (e.g. the North Atlantic Oscillation, see Chafik et al., 2019). Large uncertainties remain over the nature of shelf-wide coherent sea-level changes at sub-annual timescales, how they respond to along-isobath wind stress, and the consequences for shelf and slope circulation.

Chafik et al. (2017) showed the monthly sea-level variability on the Northwest European Shelf included a shelf-scale common mode extending from Portugal to Norway driven by atmospheric variability. Typical sea-level variations associated with the mode were of a few centimetres west of France, Ireland and the United Kingdom. Greater variations were observed in the North Sea. Chafik et al. (2017) demonstrated that this mode was related to the alignment of winds with the continental slope to the west and north of Europe. They however found regional differences, associated to different fingerprints

* Corresponding author at: The Scottish Association for Marine Science (SAMS), Scottish Marine Institute, Oban, Argyll and Bute, Scotland, UK.
E-mail address: samuel.diabate@sams.ac.uk (S.T. Diabaté).

https://doi.org/10.1016/j.csr.2025.105466
Received 12 January 2024; Received in revised form 21 March 2025; Accepted 25 March 2025
Available online 15 April 2025

of the atmospheric variability modes. Similarly, Hogarth et al. (2020) extracted the common variability in British–Irish Isles monthly tidal record residuals and presented a map of correlation with sea surface height. The common mode extended in a cross-slope sense from the shelf edge to the coast; and in an along-slope sense from south and east of the Canary Islands thousands of kilometres upstream, to the Faroe-Shetland Channel. Hogarth et al. (2020) hypothesised changes in along-slope winds were the likely driver. The Hogarth et al. (2020) and Chafik et al. (2017) modes projected differently in the southern North Sea and in the Greenland-Iceland-Norwegian basin. Nonetheless, west of France, Ireland and the UK, the two were consistent.

Chafik et al. (2017) proposed that the wind-driven on-shelf sea-level variations were reflected in changes in the eastern boundary slope current circumnavigating the European shelf through geostrophic adjustment. The mechanism linking the wind-driven shelf sea-level variability and boundary circulation is relatively simple — at least for largely subinertial flow. It is that of winds accumulating (removing) water onto (from) the shelf through Ekman transport, rising (lowering) shelf sea elevation and creating an across-slope pressure gradient. Geostrophic equilibrium suggests a boundary current balances this gradient. The cross-slope position of such a current depends on the exact response of the slope and shelf sea level to the wind forcing, with bottom friction playing a role (Huthnance, 1986a).

While it is clear that Ekman currents lead to accumulation (removal) of water onto (from) the shelf and affect the on-shelf sea level, the study of the associated acceleration or deceleration of longshore geostrophic flow is often omitted. In recent decades, a number of observational programs have measured the circulation variability around the European margin, providing means to fill this knowledge gap. In the present contribution, we characterise the shelf-wide coherent sea-level changes at sub-annual timescale, identify how they are a response to the stress imposed by along-isobath winds, and investigate the consequences for the shelf and slope circulation. We focus on timescales shorter than a year but large with respects to the inertial frequency. Section 2 presents the data used and editing performed. An analysis of sub-annual sea surface height variability, its link with the wind changes, and its effects on currents is presented in Section 3. We discuss our results in Section 4 and we conclude in Section 5.

2. Data and method

2.1. Generalities

The Northwest European Shelf is a wide shelf. The general bathymetry of this region is presented in Fig. 1. Throughout this paper, we use the following limits to define bathymetry regions west of France, Ireland and the United Kingdom. The abyssal plain and the continental rise are defined as regions where water depth exceeds 2000 m. The lower, intermediate and upper slope range from 2000 m to 1000 m, from 1000 m to 500 m, and from 500 m to 200 m respectively. The shelf-edge at 200 m separates the upper slope and the shelf. We further separate the shelf into the outer-shelf (depth>100 m) and the inner-shelf (100 m>depth>0 m). The definition of the shelf-edge at 200 m is rather classic (*e.g.*, Xu et al., 2015) and this depth approximately corresponds to where the across-isobath slope changes dramatically. Finally, upstream and downstream are meant with respect to the propagation of coastally trapped waves. In this eastern boundary context, upstream is always equatorward and downstream, poleward.

2.2. Sea level and surface geostrophic currents

The sea surface height above geoid was retrieved from the Copernicus Marine Environment Monitoring Service (CMEMS) SEALEVEL_EUR_PHY_L4_MY_008_068 regional product, available at https://doi.org/10.48670/moi-00141. This product was previously used in a recent study of the Rockall Slope Current and Rockall Trough transport (Fraser et al., 2022). It has a horizontal spacing of $1/8^\circ \times 1/8^\circ$ obtained through optimal interpolation merging of processed along satellite track altimeter measurements and covers the period 1st January 1993–31st December 2021. These processed along-track inputs have numerous corrections already applied. These include de-tiding, dynamical atmospheric correction (DAC), and more (Pujol et al., 2023). For the frequency band considered in the present work, the DAC consists solely of an adjustment for the inverse-barometer effect.

Although distributed with daily timesteps and on a $1/8^\circ \times 1/8^\circ$ grid, the altimetry data has coarse effective spatial and temporal resolution due to the mapping methodology and the satellite constellation configuration. Ballarotta et al. (2019) found effective temporal resolution to lie between 14 and 28 days around northwest Europe for a global daily SSH product with $1/4^\circ \times 1/4^\circ$ spatial grid (see their Fig. 3). To the best of our knowledge, there is no estimate of effective temporal resolution for the European regional product, but it can be anticipated to be equivalent or marginally better. For this reason, we restrict our attention to cycles longer than 20 days. Pujol et al. (2023) report, for the $1/8^\circ \times 1/8^\circ$ product we use, effective spatial resolutions of 200 km or less west of France, Ireland and the UK (see their Figure 15). For context, the shelf has a cross-slope width ranging from ~50 km off Erris Head (Ireland, 10°0.2W, 54°18.4N) to ~400 km off the tip of Cornwall (UK).

Sea surface height derived from satellite altimetry can be problematic at immediate proximity of the coastline. To validate our results, we retrieved tide gauge monthly timeseries from the Permanent Service for Mean Sea Level (Permanent Service for Mean Sea Level, 2023; Holgate et al., 2013, dataset downloaded on 13th February 2023). We only make use of Revised Local Reference (RLR) data, and select tide gauges with no more than 20% missing values over a lifespan of at least 10 years within the 1993–2022 period. Additionally, we obtained from the Irish National Tide Gauge Network (INTGN) tidal records from three tide gauge sites located along the coast of the Republic of Ireland. These records are unavailable on the PSMSL website but match the above criteria of completeness and duration. They are Howth, at proximity of Dublin in the Irish Sea; Castletownbere southwest of Cork; and Galway, facing the open Atlantic ocean. A static inverse barometer contribution is removed from all tide gauge records.

2.3. Atmospheric sea-level pressure and winds

Daily mean horizontal wind speeds at 10 m above the mean sea surface were obtained from The NCEP/DOE AMIP-II Reanalysis (Kanamitsu et al., 2002, NOAA PSL, Boulder, Colorado, USA, https://psl.noaa.gov, last access: 08 August 2022) for the period January 1993–December 2021 and converted to wind stresses.

Monthly mean surface pressure, also obtained from the NCEP/DOE AMIP-II Reanalysis (Kanamitsu et al., 2002), were used to correct the tide gauge records for the inverse barometer effect, assuming an isostatic response.

2.4. In-situ currents from moored deployments

Our analysis relies on data from Single-Point Current-Meters (SPCMs) and Acoustic Doppler Current Profilers (ADCPs) moored on the shelf and slope west of France, the Republic of Ireland, and the United Kingdom. We restrict our attention to deployments carried out since the start of the altimetry era in 1993, for comparison with sea surface height. ADCP and SPCM data were obtained from numerous historic and ongoing observational programs, including new data from the recent Irish Ocean Observing System (EirOOS). Details on mooring data are given in Appendix A.

Modern ADCPs and SPCMs internally perform a non-negligible level of initial editing including coordinate transform, quality control and ensemble averaging. The data obtained after this initial editing is an ideal and sufficiently upstream source. We then perform the following

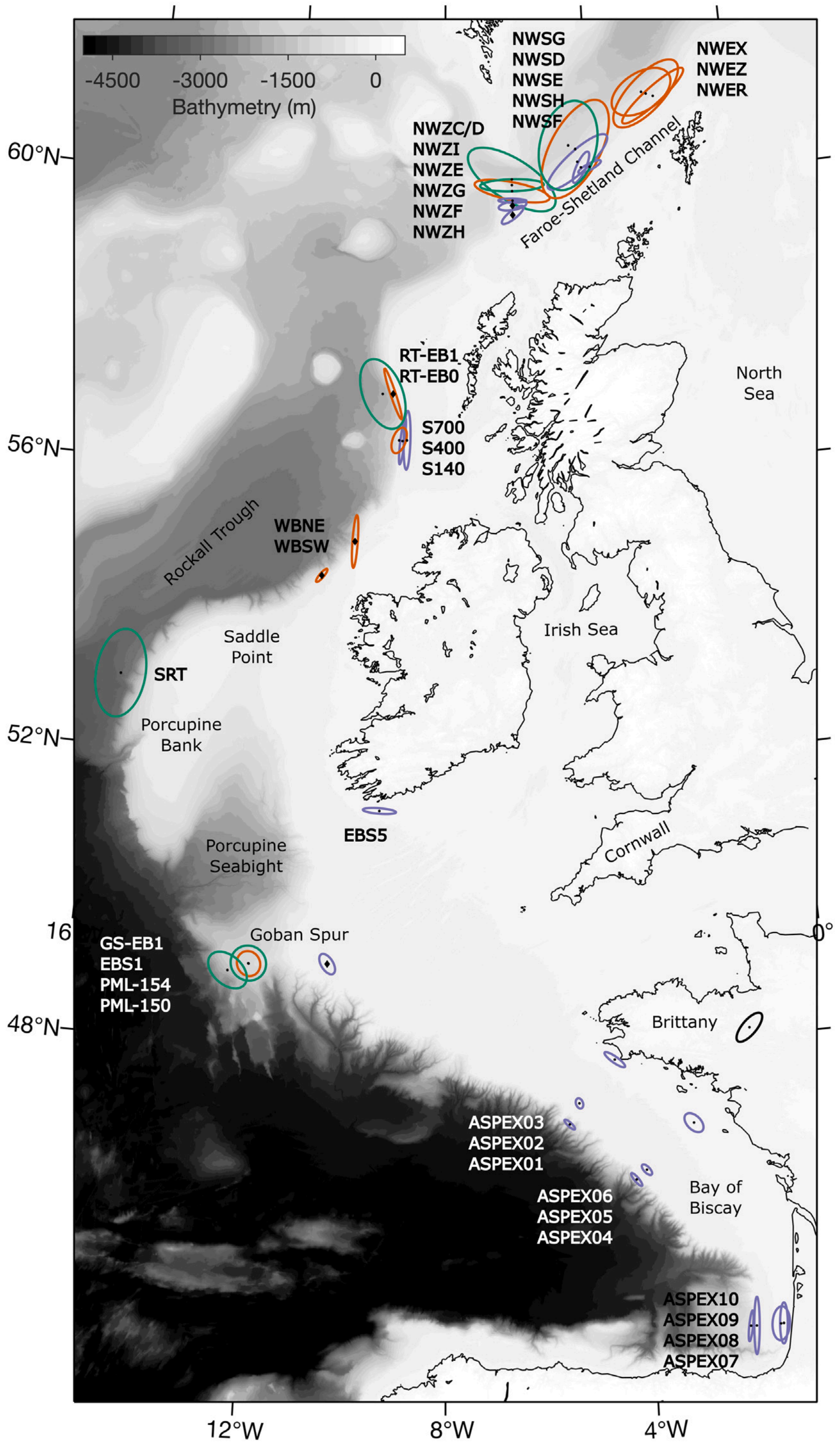

Fig. 1. Bathymetry maps with markers indicating mooring positions and standard deviation ellipses of 20-day low-pass filtered in-situ current variability. The reference ellipse at 01°41E, 48°07N has a semimajor axis radius of 5 $\mathrm{cm \cdot s^{-1}}$ and a semiminor axis radius of 2 $\mathrm{cm \cdot s^{-1}}$. Moorings above the shelf and upper slope are indicated in purple, the ones over the intermediate slope in orange, and moorings in deeper waters are shown in green. At mooring sites indicated with diamond markers, standard deviation ellipses are shown for a single depth level (see text).

processing workflow, which is a twice-repeated combination of interpolation and low-pass filtering. At each mooring site, data from sensors installed at different depths or from different deployments at the same site are merged. A depth-time interpolation based on a Delaunay triangulation allows to re-grid horizontal velocities on a regular mesh and eliminate blow-down effects. The query grid has 10-metre depth-increments and hourly timesteps. Interpolation is performed only for depth-time query coordinates falling within triangles of inter-vertex distances inferior to three hours and half the water column depth or 300 m (whichever is the largest). Query points not meeting these thresholds are omitted. The obtained horizontal velocities are convoluted with a 3-day Tukey window and daily averaged. This low-pass filters the velocities and effectively removes the tidal signal. Once de-tided, the data has considerably greater temporal auto-correlation. It is again interpolated using a Delaunay triangulation, but this time allowing for greater inter-vertex distances in time (up to ten days).

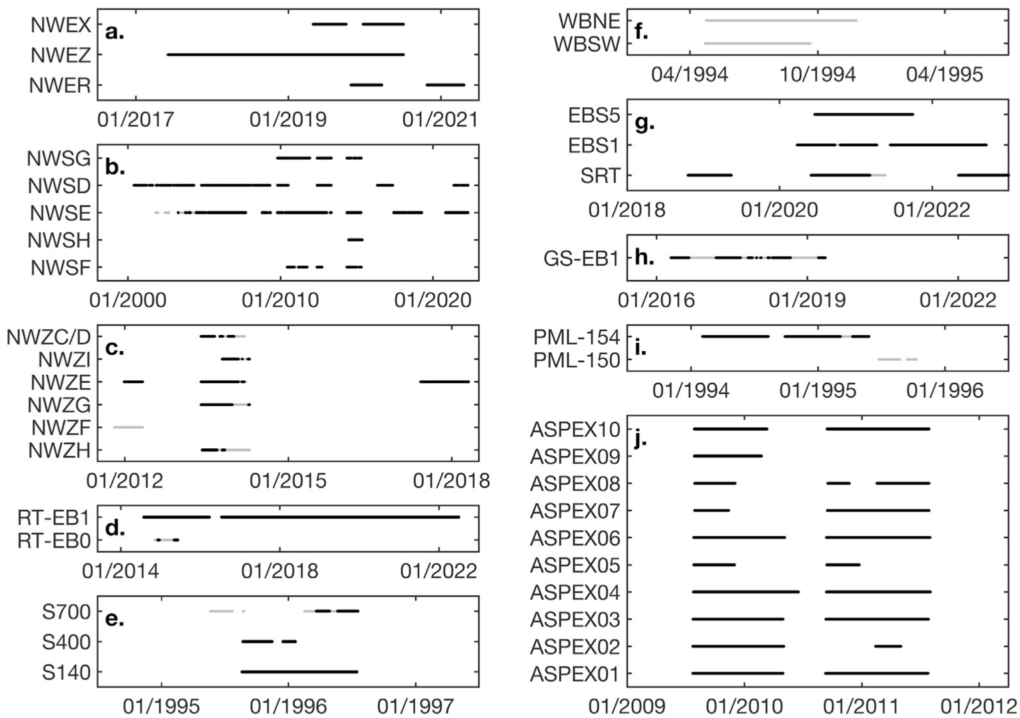

Fig. 2. Temporal coverage of each of the mooring used in the present study. Black marker indicates, for each timestep, that a depth-averaged current could be computed, while grey line indicates that although a depth average could not be obtained, some information at this mooring is available. Note limits of the x-axes are different for each panel.

Finally, the obtained velocities are convoluted with 20-day Tukey window to focus on low-frequency variability and for consistency with the sea surface height data. The regularly gridded and low-pass filtered currents are depth averaged from the surface to the 500 m level (or the bottom if shallower). The rationale for such averaging is that currents in the northeast Atlantic margin are very vertically coherent in this depth range. Note the gaps in the in-situ current data as well as the various deployment durations do not allow to remove seasonality or lower frequency variability. For each timesteps, if missing data represents a significant fraction of the water column (more than 50%), the whole average is considered as missing.

The above-described processing stream was performed for all mooring lines equipped with several SPCMs and/or at least one ADCP. RT-EB0, NWZF and NWZH are three mooring sites equipped with bottom mounted upward-looking ADCP which do not meet our completeness threshold for extended amounts of time. For these moorings, we swap the depth-average estimates for currents at a given depth level instead (respectively, 500 m, 180 m and 160 m). Lastly, we augment our dataset with three mooring sites with data available from only one SPCM, but which fill in geographical gaps. They are OMEX moorings WBNE, WBSW and PML-150 (see Appendix A). For these moorings, velocities are simply binned at a nominal depth and convoluted with a 20-day Tukey window. Table 1 presents a summary of all 36 mooring data used, and Fig. 2 presents temporal coverage for each mooring individually.

In Fig. 1 current standard deviations, obtained through principal component decomposition (see Appendix C), are represented as ellipses. The semi-major and semi-minor ellipse radii indicate the amplitude of the standard deviation of current deviations from the mean flow. The semi-major axis orientation indicates the principal direction of variance. The currents show considerable variance at all sites, also with a poleward increase in magnitude. The main direction of variance is everywhere aligned with local isobaths. We observe a greater topographical steering at slope and coastal mooring sites than at outer-shelf and abyssal locations. The peculiar bathymetry of the Goban Spur leads to a singular zone where little topographical steering can be observed, with the variance ellipse making up an almost perfect circle at EBS1 (approx. 12°E, 49°N). The same observations can be drawn from the record obtained from PML-154 mooring, which was also located above the 1000 m isobath on the Goban Spur (the two mooring positions coincide, but there are 20+ years between deployments).

2.5. *In-situ currents from underwater gliders*

In recent years, the Overturning in the Subpolar North Atlantic Program (OSNAP) has integrated underwater glider observations, which are used to accurately estimate hydrography and transport at the eastern boundary of the array (Fraser et al., 2022). The gliders cross the slope from the RT-EB1 mooring position above a depth of ~1800 m, to the shelf edge and allow for an unprecedented spatial resolution. Fraser et al. (2022) derived along-slope velocity estimates from the thermal wind shear referenced to the mean horizontal velocity derived from the glider deflection off course between consecutive GPS fixes. The nominal resolution of their product is $dx = 250$ m. The effective horizontal resolution is determined by the distance between repeated glider dives/ascent and is on the order of 3 km. It gets better with shallowing bathymetry, as can be seen on Figure 2b of Fraser et al. (2022). The temporal resolution is on the order of two transects per week. We interpolate (Fraser et al., 2022) estimate on regular time intervals by employing an inverse distance-weighting technique, where the power parameter is set to $p = 2$ and a 20-day search radius is used. The velocities are then depth-averaged, and, to focus on the low-frequency variability, convoluted with a 20-day Tukey window.

3. Analysis

3.1. *Shelf sea-level variability and associated geostrophic flow*

The altimetry-derived sea-level anomaly η is objectively decomposed into variability modes using empirical orthogonal function analysis,

$$\eta(x, y, t) = \sum_{i=1}^{n} \phi_i(x, y)\alpha_i(t), \tag{1}$$

Table 1
Summary of mooring data used. Longitudes and latitudes are given in degrees–decimal minutes. Depths are averaged in case of several deployments, and approximated to the nearest ten. BODC is the British Oceanographic Data Centre. ENVOFAR is the Environmental Data on Terrestrial and Marine Ecosystems in the Faroe Islands. Pers. Com. indicates personal communication.

Program	Name	Location	Depth (m)	Source	Publication(s)
Faroe-Shetland Channel					
–	NWER	02°05.4 W, 61°07.4N	490	Pers. Com.	–
–	NWEZ	02°17.5 W, 61°09.3N	630	Pers. Com.	–
–	NWEX	02°25.0 W, 61°11.0N	730	Pers. Com.	–
–	NWSF	04°00.1 W, 60°12.0N	170	Pers. Com.	Berx et al. (2013), Hansen et al. (2013)
–	NWSH	04°14.4 W, 60°11.9N	200	ENVOFAR	Berx et al. (2013), Hansen et al. (2013)
–	NWSE	04°20.3 W, 60°16.6N	450	Pers. Com.	Berx et al. (2013), Hansen et al. (2013)
–	NWSD	04°22.5 W, 60°27.2N	810	Pers. Com.	Berx et al. (2013), Hansen et al. (2013)
–	NWSG	04°33.9 W, 60°29.7N	1050	Pers. Com.	Berx et al. (2013), Hansen et al. (2013)
–	NWZH	06°10.0 W, 59°36.0N	210	Pers. Com.	–
–	NWZF	06°09.9 W, 59°42.3N	210	Pers. Com.	Hansen et al. (2013)
–	NWZG	06°09.9 W, 59°46.4N	370	Pers. Com.	Hansen et al. (2013)
–	NWZE	06°10.1 W, 59°54.4N	780	Pers. Com.	Hansen et al. (2013)
–	NWZI	06°10.0 W, 59°59.2N	1010	Pers. Com.	Hansen et al. (2013)
–	NWZC/D	06°10.1 W, 60°04.0N	1100	Pers. Com.	Hansen et al. (2013)
Hebridean and Malin Seas					
OSNAP	RT-EB0	09°20.3 W, 57°06.2N	750	Pers. Com.	Fraser et al. (2022), Houpert et al. (2020)
OSNAP	RT-EB1	09°36.0 W, 57°06.0N	1800	Pers. Com.	Fraser et al. (2022), Houpert et al. (2020)
LOIS-SES	S140	08°58.0 W, 56°28.0N	140	BODC	Souza et al. (2001), Xu et al. (2015), Huthnance et al. (2022)
LOIS-SES	S400	09°04.8 W, 56°27.2N	400	BODC	Souza et al. (2001), Xu et al. (2015), Huthnance et al. (2022)
LOIS-SES	S700	09°09.8 W, 56°27.7N	700	BODC	Souza et al. (2001)
OMEX	WBNE	10°12.0 W, 55°02.5N	655	BODC	White and Bowyer (1997)
OMEX	WBSW	10°58.1 W, 54°33.2N	668	BODC	White and Bowyer (1997)
West and southwest of Ireland					
EirOOS	SRT	15°31.2 W, 52°59.9N	3010	–	–
OMEX	PML-150	10°30.9 W, 49°09.0N	140	BODC	Pingree et al. (1999), Huthnance et al. (2001), van Aken et al. (2005)
OMEX	PML-154	12°10.8 W, 49°06.5N	1000	BODC	Pingree et al. (1999), Huthnance et al. (2001), van Aken et al. (2005)
EirOOS	EBS5	09°28.2 W, 51°18.0N	90	–	–
EirOOS	EBS1	12°11.1 W, 49°06.8N	990	–	–
NOAC	GS-EB1	12°37.1 W, 49°00.0N	1530	Moritz et al. (2021a)	Moritz et al. (2021b)
Bay of Biscay					
ASPEX	ASPEX01	04°30.2 W, 47°47.7N	70	Pers. Com.	Le Boyer et al. (2013), Kersalé et al. (2016)
ASPEX	ASPEX02	05°16.0 W, 47°12.6N	130	Pers. Com.	Le Boyer et al. (2013)
ASPEX	ASPEX03	05°28.9 W, 46°55.4N	460	Pers. Com.	Le Boyer et al. (2013)
ASPEX	ASPEX04	02°57.3 W, 46°51.6N	50	Pers. Com.	Le Boyer et al. (2013), Kersalé et al. (2016)
ASPEX	ASPEX05	03°58.1 W, 46°15.0N	140	Pers. Com.	Le Boyer et al. (2013)
ASPEX	ASPEX06	04°11.0 W, 46°7.3N	420	Pers. Com.	Le Boyer et al. (2013)
ASPEX	ASPEX07	01°30.8 W, 44°00.1N	50	Pers. Com.	Le Boyer et al. (2013), Kersalé et al. (2016)
ASPEX	ASPEX08	01°34.0 W, 43°59.9N	70	Pers. Com.	Le Boyer et al. (2013)
ASPEX	ASPEX09	02°01.9 W, 44°00.0N	140	Pers. Com.	Le Boyer et al. (2013)
ASPEX	ASPEX10	02°08.6 W, 44°00.1N	460	Pers. Com.	Le Boyer et al. (2013)

after a 20–360 day bandpass filter is applied at each gridpoint. The modes are ordered by decreasing importance, associated to the fraction of total variance they explain individually. For details on EOF technique, see Appendix B. The North Sea is not considered, to focus on the variability to the west of the UK, Ireland and France. The bandpass filtering method removes the mean seasonal cycle in the sea surface height data, but does not correct for any seasonal cycle in the variance or higher-moment statistics. This minor problem is discussed in Appendix E. The time-varying principal components (PCs) α and spatially varying empirical orthogonal vectors or functions (EOFs) ϕ together make up the modes $i = 1, 2, 3, \ldots, n$. To focus on coherent signal of large spatial scale in sea surface height field, we discuss the leading mode $i = 1$, associated with the pair $\phi_1 \cdot \alpha_1$. Note that principal component analysis is well-known to be dependent on the domain extent and on spatial differences in variance and skewness (Monahan et al., 2009). Here, we decided to exclude the North Sea from our analysis because its variability is different from the region west of France, Ireland and the UK. For example, the two regions are affected differently by atmospheric mode teleconnections (Chafik et al., 2017). These differences are not easily captured using (covariance-based) EOF decomposition because the sea-level variance in the North Sea is much greater than (say) west of France.

Fig. 3a shows the leading EOF ϕ_1, which is positive over the entire shelf. This represents the in-phase, coherent sea-level variations. The general picture is that of maximum amplitudes at the coast and gently decaying oceanward, up to the slope where they vanish ($\phi_1 \sim 0$). Broadly speaking, ϕ_1 follows bathymetry contours, with some bathymetric features distinguishable (Goban Spur, Porcupine Seabight, Porcupine Bank, the gentle slope of the outer Celtic shelf, etc.). In addition, ϕ_1 increases poleward along the coast, with maximum values found in the northern Irish Sea and on the inner Scottish shelf. In total, the mode accounts for 16% of the sea surface height variance over the domain, but the fraction of variability explained is much greater over the shelf, particularly around Ireland and west of the UK (Fig. 3b., we return to this point further below). On the other hand, the open ocean variability is largely unexplained by the mode (Fig. 3b.) — and reversely, the open ocean makes little contribution (Fig. 3a.). This is expected, because at the timescales considered here, the open ocean sea surface height variability largely reflects eddying activity which is not coherent over large spatial regions.

The horizontal gradients of ϕ_1 are associated with surface geostrophic anomalous currents which can be readily derived using

$$\boldsymbol{v} = -g\boldsymbol{k} \times \nabla(\phi_1)/f, \tag{2}$$

where $\boldsymbol{k}$ is the unitary vertical vector. The velocities are generally orientated along-isobath and increase poleward in magnitude (Fig. 3c). The anomalous currents flow poleward when the sea-level anomaly is positive over the shelf. Northwest of Ireland as well as west and north of Scotland, broad, strong currents can be observed. There, strong velocities encompass the whole shelf. They also encompass a significant part of the slope. However, this feature is likely introduced by the optimal interpolation involved in the generation of the gridded sea

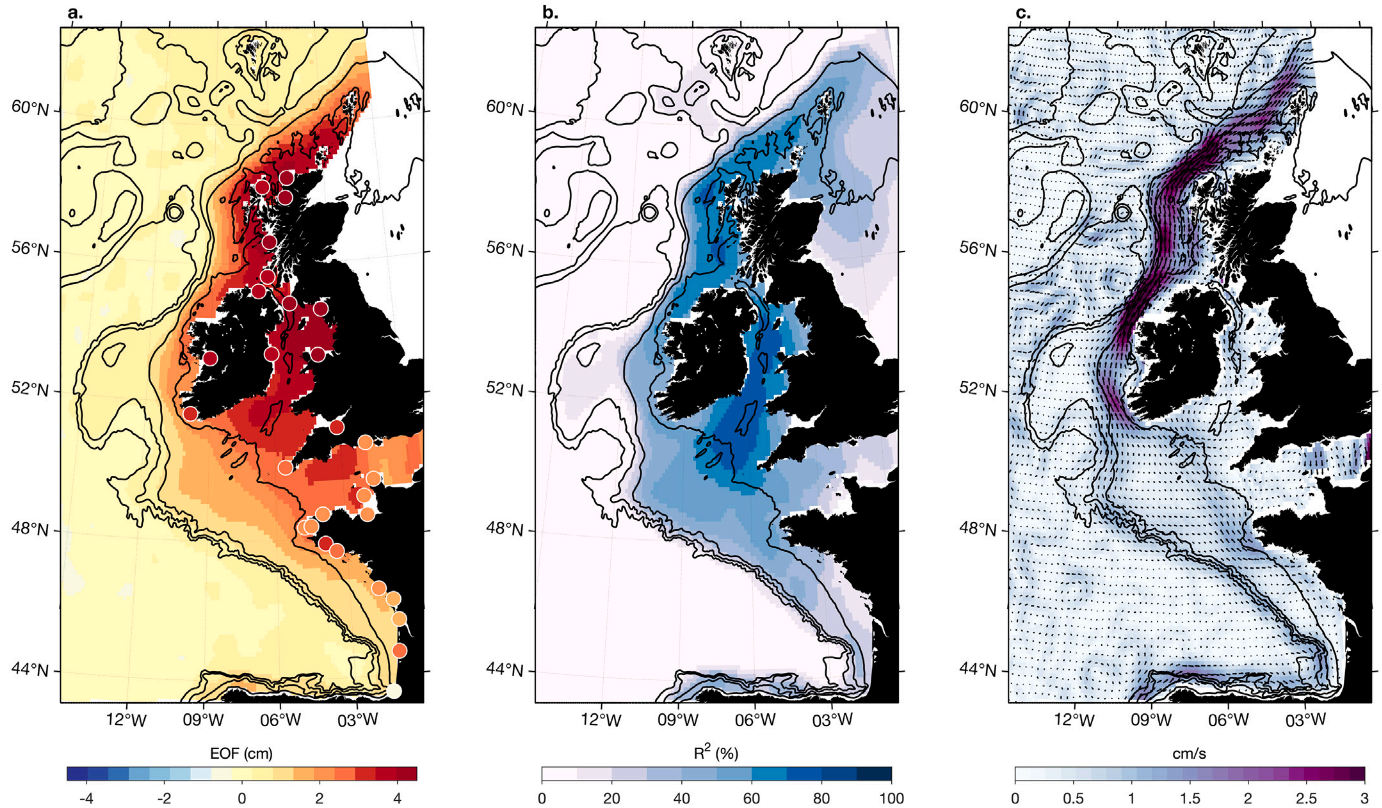

Fig. 3. (a) The leading covariance-based EOF ϕ_1 of sea surface height anomaly over the domain (colour shadings). (b) The variance explained (in percent) by the leading principal component α_1 at each grid point, obtained by squaring the correlation between α_1 and local sea surface height changes. (c) The surface geostrophic currents associated with the mode, $\boldsymbol{v} = -g\boldsymbol{k} \times \nabla(\phi_1)/f$. On (a), coloured circular markers present the regression coefficients of the tide gauge timeseries versus the principal component α_1. On all three maps, black contour lines indicate bathymetry levels 100 m, 200 m (the shelf-edge), 1000 m and 2000 m.

surface height product which tends to smooth sharp sea surface height gradients, typically found above sharp bathymetry gradients. From 54°N to 51°N, strong current anomalies are limited to the east of the saddle point and Porcupine Seabight — they do not extend around the Porcupine Bank. From 51°N to the southern Bay of Biscay, current anomalies are diffuse and relatively weaker than to the north. In this region there exists two distinct circulation patterns associated with the mode: a coastal pathway perceptible along the Brittany coast, west of the tip of Cornwall and flowing towards Ireland, and a well separated slope pathway.

The associated principal component α_1 is shown in Fig. 4a. It explains between 40 and 80% of the sea surface height variability over the shelf north of 47° N (Fig. 3b.), which indicates its usefulness to help the analysis of shelf sea-level variability and, we argue, current changes. It features important fluctuations, putting in perspective the values taken by ϕ_1 and $\boldsymbol{v}$ which are relative to periods when $\alpha_1 = 1$. The peak-to-peak amplitude (maximum value minus minimum value) of α_1 is ~ 8.4, associated to ±14–20 cm sea-level change in the northern Irish Sea and along the western Scottish coast and up to ±15 cm·s^{-1} surface geostrophic current change northwest of the Outer Hebrides. However, this range reflects extremum positive and negative figures which occurred only once over the observation period. In Fig. 4b and c we present the distribution of values taken by α_1, together with its probability of being below a given threshold (which is simply the accumulated distribution). One week per year on average, the principal component is found above a value of + 2, associated with sea elevation ≥9 cm above the background state in the northern Irish Sea and Scottish inner-shelf and anomalous surface geostrophic current ≥7 cm·s^{-1} northwest of the Outer Hebrides. A week every ten years, the principal component is above + 3, that is an anomalous sea elevation ≥10 cm and anomalous surface geostrophic currents ≥11 cm·s^{-1} in the same regions.

To show that the shelf common mode extends all the way to the coastline, the tide gauge timeseries were regressed against the monthly-averaged principal component α_1. Prior to this operation, the tide gauge records were linearly detrended, their seasonal climatological cycle was subtracted and a 11-month running mean (tolerant to missing values) was removed. The obtained regression coefficients, shown as circular markers in Fig. 3a represents how much sea-level variability within this mode projects to the coast. The markers are almost identical to their nearestmost ϕ_1 value, indicating the relevance of the common mode even at the coastline.

3.2. Source of the shelf variability

Numerous studies have highlighted the role of winds in driving Northwest European Shelf variability throughout a range of timescales (Gordon and Huthnance, 1987; Chafik et al., 2017; Pingree and Le Cann, 1989; Pingree et al., 1999; Le Boyer et al., 2013; Plag and Tsimplis, 1999; Hermans et al., 2020; Calafat et al., 2012; Chafik et al., 2019). Therefore, we compare in this section the coherent sea surface height variability associated with $\phi_1 \cdot \alpha_1$ with changes in the atmospheric circulation.

The physical response of the ocean to the wind stress action yields the observed sea-level variability $\alpha_1(t)$. We model this process as a linear and time-independent response (we effectively assume $\alpha_1(t)$ is fully wind driven),

$$\alpha_1(t) = \frac{1}{S} \iint_S \boldsymbol{K}(x, y) \cdot \boldsymbol{\tau}(x, y, t)\, dx dy, \tag{3}$$

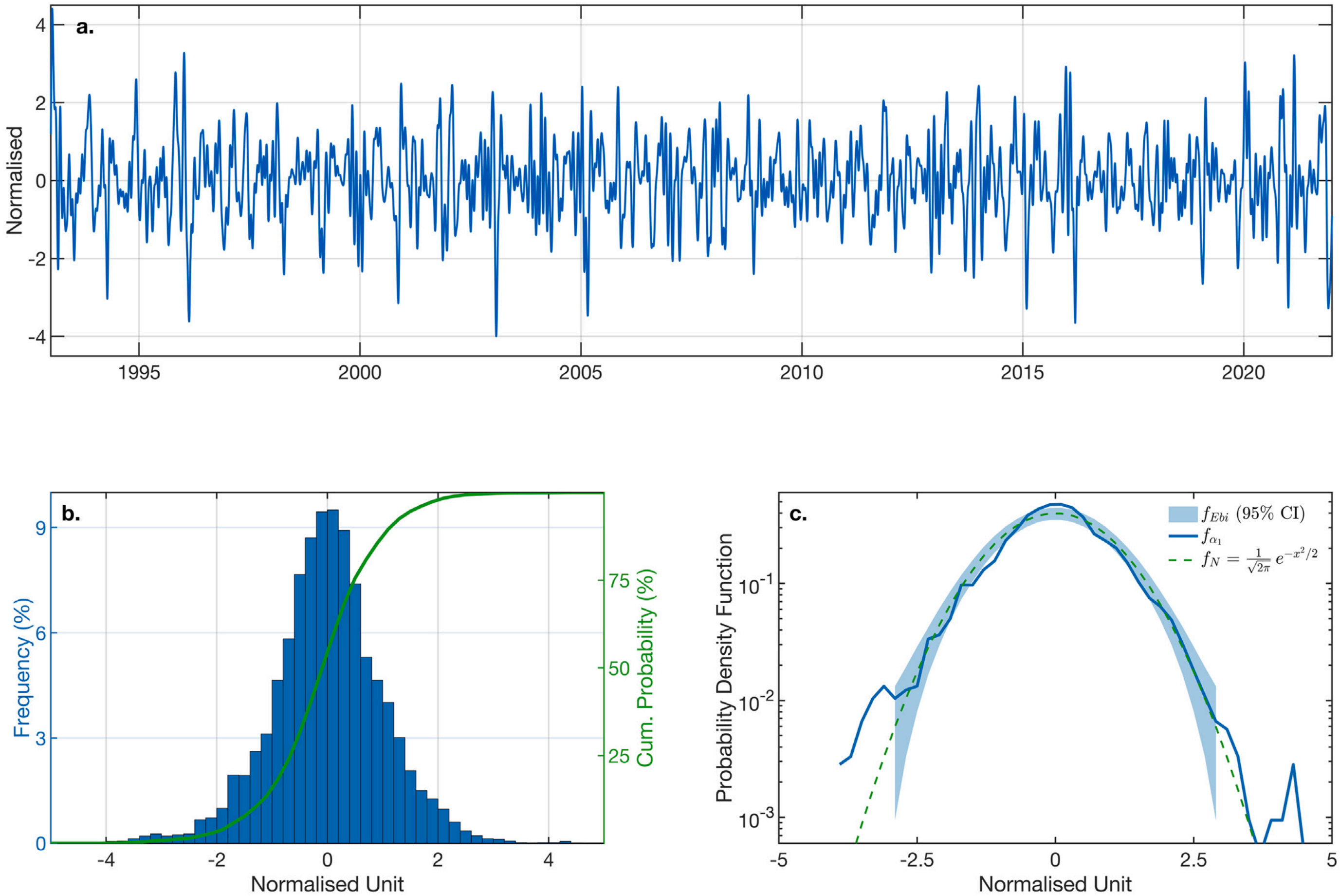

Fig. 4. (a) The leading principal component α_1 or timeseries of the mode. (b) The histogram of α_1 (blue bars), and the associated probability of α_1 being below a given threshold (green line). (c) Estimated probability density function f_{α_1} in logarithmic scale (dark blue line), together with 95% confidence interval of randomly obtained probability density function f_{Ebi} (light blue area), and the standard normal distribution probability density function (dashed green line). Note the timeseries randomly created using the Ebisuzaki (1997) method and used to test significance have a distribution which is approximately normal (Panel c.).

where $\boldsymbol{K} = (K^x, K^y)$ is a vector field representing the sensitivity of α_1 to the surface wind stress anomaly $\boldsymbol{\tau} = (\tau^x, \tau^y)$ at any given point (x, y). This sensitivity is sought using a Principal Component based Multiple Linear Regression approach (PCMLR, see Appendix D below and Mendeş, 2009).

Fig. 5a presents $\boldsymbol{K}$, the sensitivity of the ocean to the forcing action of the wind stress changes. Over the shelf and slope to the south of Ireland and west of France, large $\boldsymbol{K}$ vectors aligned with isobaths are seen. They are significant above 99% threshold (details on how significance is obtained are given in Appendix D). On Fig. 5 b. to d., we present the wind-based reconstruction of the shelf sea-level variability obtained with Eq. (D.1) after masking out non-significant grid-points and grid-points outside of the 18° W, 44° N to 00° W, 60° N box. This reconstruction compares very favourably with α_1 (correlation is $r = 0.66$). Altogether, these results highlights that along-isobath winds in the shelf and slope regions to the west of France and south of Ireland are the primary driver of changes in α_1.

3.3. Response of currents to sea surface height changes

We now investigate whether the sea surface height changes associated with the mode $\phi_1 \cdot \alpha_1$ also feature in in-situ current observations. Correlation between the common mode principal component α_1 and the along-isobath component of depth-averaged in-situ velocities is presented in Fig. 6. Since no attempt was made to account for the seasonal cycle or any lower frequency variability in in-situ current observations — the shortness of the records hinders such procedure —, correlation values should be looked as conservative estimates. Significance, shown as black dots in Fig. 6 was tested following the Ebisuzaki (1997) method. Ten thousand randomly created timeseries were correlated against the along-isobath component of depth-averaged in-situ velocities. When less than five percent of the randomly generated correlations are larger than the true correlation, the agreement is deemed significant.

Fig. 6 highlights great agreement from the Goban Spur to the Faroe-Shetland Channel between α_1 and current variability over the upper-slope and outer-shelf. In the Faroe-Shetland Channel (Panel a.), high correlations are seen at NWSF, NWSH, NWZH, and NWZF (r = 0.43, 0.58, 0.59 and 0.55 respectively, all significant). A visual inspection of the velocity timeseries together with that of the common mode principal component α_1 highlight differences but general agreement (Fig. 7a and b). On the Hebridean slope (Fig. 6 b.), correlations and significance between α_1 and the depth-averaged along-isobath velocities obtained from the repeated glider transects at 57°N (Fraser et al., 2022) increase almost monotonically with decreasing depth up to a maximum value at the shelf edge (∼ 200 m). Significant correlations (above 95%) are found within one kilometre of the shelf-edge, approximately corresponding to correlation superior to 0.35. In effect, the glider-obtained velocities averaged in the 365–195 m isobath range show periods of strong agreement with the common mode (*e.g.*, June–July 2020, October 2020–January 2021, November 2021) and a period of no agreement at all (April–May 2021, see Fig. 7c.). The elevated and outlying spring 2021 velocity values can be related to the presence

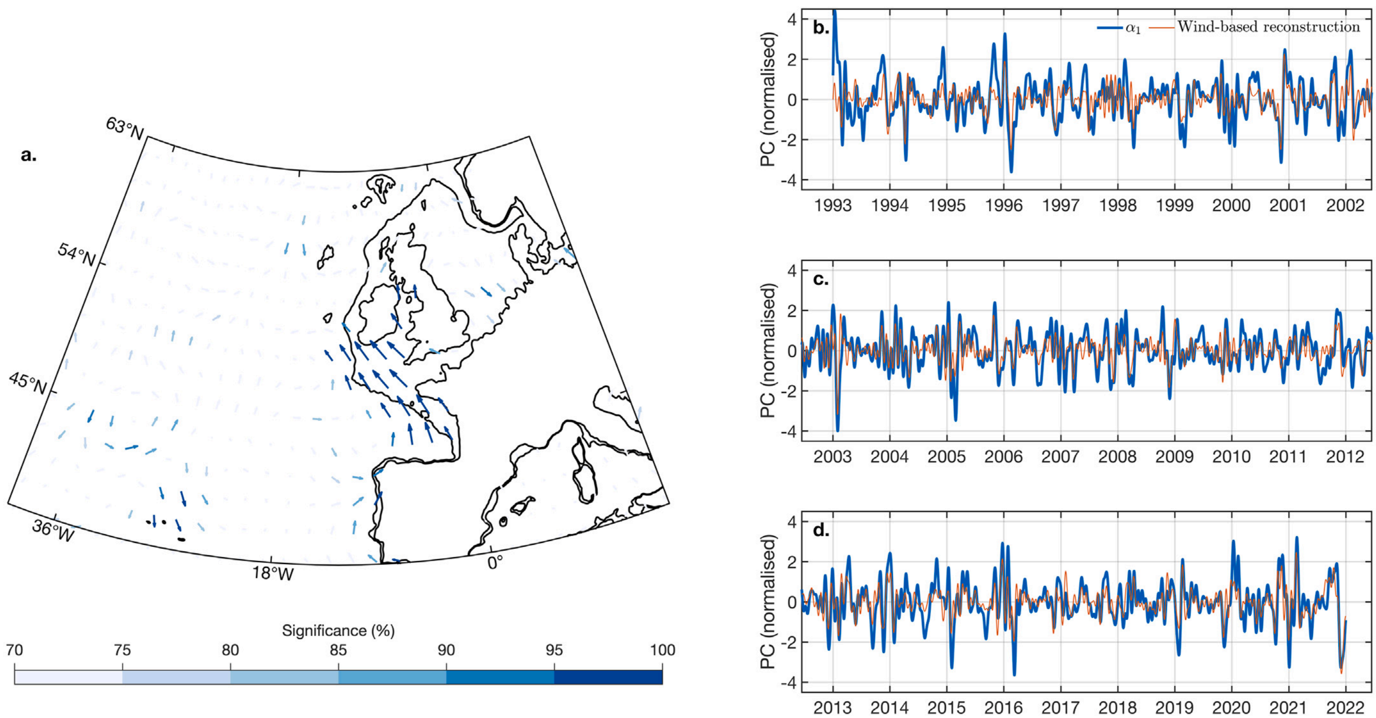

Fig. 5. (a) The sensitivity $\boldsymbol{K}(x, y)$ of shelf sea-level changes — more exactly, α_1 — to wind stress variations in the Northeast Atlantic. Significance, which is obtained using a modified Ebisuzaki (1997) approach (see text), is indicated as shades of colours. This map should be read recalling the dot product in Eq. (3). When wind stress anomaly vectors exactly 'line-up' with $\boldsymbol{K}$, the shelf sea level is high. At the other extreme, during period when wind stress anomaly vectors oppose $\boldsymbol{K}$, largely negative sea levels are obtained over the shelf. When the wind field is in no particular arrangement with respect to $\boldsymbol{K}$, the principal component α_1 takes values closer to zero. (b, c and d) The sea-level mode principal component α_1 is shown as a blue line together with the wind-based fit, which is obtained by summing wind stress anomalies projected along the sensitivity $\boldsymbol{K}$, retaining only significant (> 95%) grid points in the box 18° W, 44° N to 00° W, 60° N (orange line).

of two consecutive and long-lived eddies in the zone, also observed at RT-EB1 (See Figure 16.10 of Moat et al., 2022). Farther south, at 56°28N, depth-averaged flow at S140 and S400 agree well with the common mode, with correlation of r = 0.47 and r = 0.78 respectively, significant at 98% and >99% (Fig. 6b and Fig. 7d.). Southwest of Ireland, a strong correlation is seen between α_1 and the along-isobath currents measured by the upper SPCM (30 m below surface) at PML-150 r = 0.65, significance is 93%, only slightly below the 95% threshold, see Fig. 6c and Fig. 7d.).

During the September 1995–October 1995 period, increase in along-isobath anomalous flow at PML-150 on the Goban Spur outer-shelf was concurrently observed at S400 and S140 on the Hebridean upper slope and outer shelf (Fig. 7 d.). During this period, α_1 went from a negative to a positive phase which was associated with sea-level rise on the shelf and translated in increased anomalous surface geostrophic currents. This further demonstrates that shelf sea-level variations are responsible for along-isobath coherence along the shelf-edge.

In the intermediate slope depth range (1000–500 m), correlations are lower (NWE line, NWSD, RT-EB0, S700, WBNE, WBSW) and in general non-significant. This reflects the lessening of the shelf sea-level influence on currents; or alternatively the increasing dominance of other sources of variability at this depth range. In even deeper water, current variability does not reflect the shelf mode at all (RT-EB1, SRT, PML-154, EBS1, GS-EB1). Finally, farther south in the Bay of Biscay, no significant agreement is found between in-situ current observations and the common mode of sea-level variations regardless of the depth range.

The general picture at the outer-shelf and upper-slope is that of an agreement between on-shelf sea-level variability and along-isobath in-situ currents from the Faroe-Shetland Channel to the Goban Spur (Fig. 6). The agreement decreases sharply with depth across the slope.

4. Discussion

We identified coherent sub-annual sea surface height changes on the shelf from the Bay of Biscay to the Faroe-Shetland Channel, well separated from the open ocean variability. The spatial fingerprint of the common sea-level variability is that of elevated amplitudes at the coastline, decaying gently across the shelf and sharply decreasing to zero magnitude offshore of the shelf-edge towards the abyssal ocean. These coherent sub-annual sea-level fluctuations are in excess of 9 cm above background mean sea level one week per year on average in the Irish Sea and along the Scottish coastline. Winds were shown to drive these shelf-wide variations, which contribute to extreme sea levels along the seaboards of France, the UK and Ireland. Specifically, the alignment of winds with local isobaths in the region west of France and south of Ireland was found to play a key role.

Our analysis shares some similarity with past works that focused on the monthly sea-level variability over the Northwest European Shelf (Chafik et al., 2017; Hogarth et al., 2020). Chafik et al. (2017) suggested the coherent shelf sea-level variability drove changes in the boundary circulation, but this was never checked with in-situ data as was done here. We generally found that, as hypothesised by Chafik et al. (2017), depth-averaged currents over the outer-shelf and upper-slope balance the coherent shelf sea-level changes from the Goban Spur to the Faroe-Shetland Channel. The along-isobath velocities at SES sites and Faroe-Shetland Channel moorings were known to be in agreement with local surface geostrophic flow (Xu et al., 2015; Berx et al., 2013), but we highlight the specific role of the common shelf sea-level variability in driving the outer-shelf and upper-slope geostrophic circulation, which is not simply local and extends thousands of kilometres along isobath. This was not previously shown.

The general physical mechanism is that shelf sea-level variations, established from the mass convergence and divergence associated to the wind-driven Ekman transport, must be balanced by the Coriolis

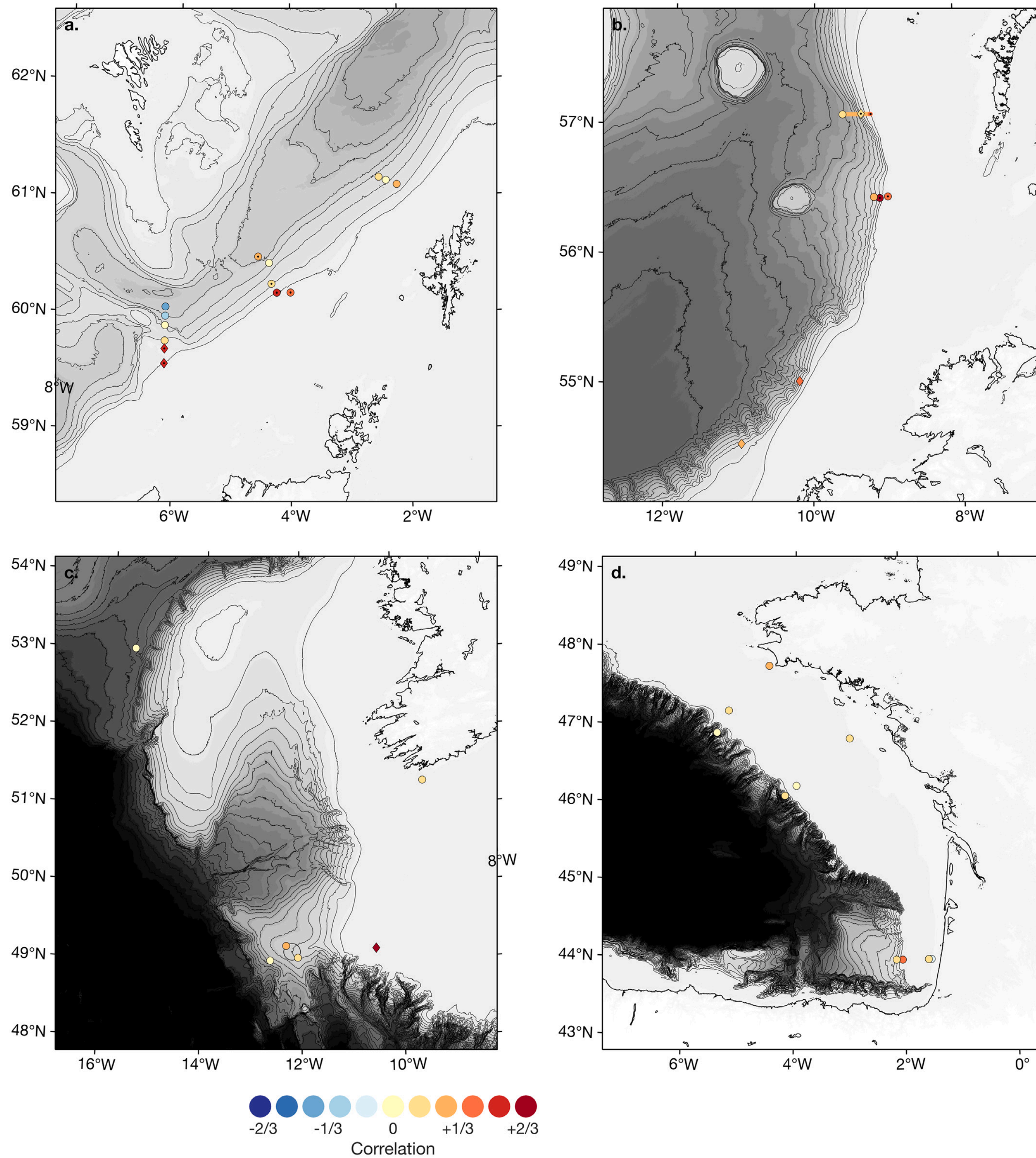

Fig. 6. Correlation between depth-averaged in-situ velocities projected along-isobath and the common mode principal component α_1 in the four regions (circular markers). Diamond markers indicate correlations obtained with velocities measured at a single level rather than with depth-averaged currents (see text). Significance above the 95% level is indicated by black dots. In (c), PML-154 and EBS1 on the Goban Spur are, for readability, shown displaced from their original position (the central dot). Correlations with velocities obtained from Fraser et al. (2022) glider section are also shown on (b), underneath the mooring markers. On all panels, isobaths are indicated every 200 m by thin black contours.

force. This means that elevated sea levels on the shelf lead to accelerated geostrophic along-isobath currents. In practice, the winds set up coastally trapped waves, but, at long enough timescales, development is nil ($\partial_t \sim 0$), and these waves are arrested. Simply put, this means the characteristic wave speeds are considerably faster than the wind changes, so that an equilibrium is reached virtually instantaneously, and the timescale of changes in sea level and currents is imposed by the wind forcing. The spatial structure of ϕ_1 — roughly a function of the seabed depth alone, with amplitudes maximum at the coast, decaying gently oceanward and abruptly vanishing at the slope —

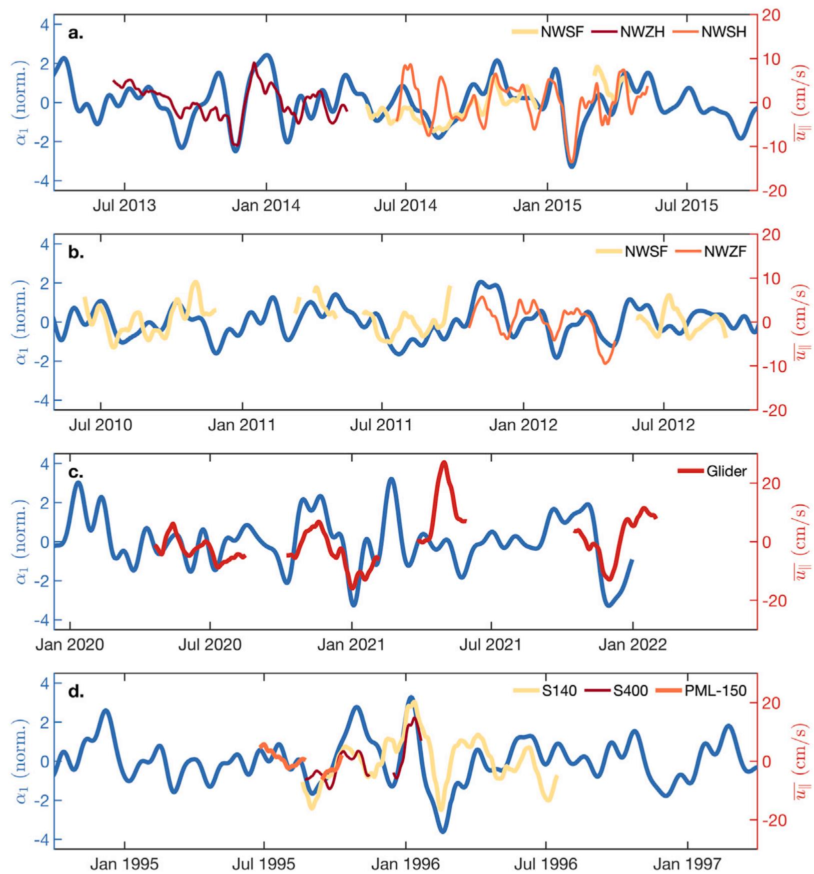

Fig. 7. Principal component α_1 against in-situ along-isobath current anomalies. Currents are depth-averaged everywhere, except for moorings PML-150, NWZH, and NWZF (see text). On c., glider-obtained depth-averaged velocities are averaged over the 365–195 m isobath range.

reminds of the characteristic fingerprints of continental shelf waves. Continental shelf waves are shelf topographic Rossby waves (Gill and Clarke, 1974; Mysak, 1980; Huthnance, 1986a; Gordon and Huthnance, 1987; Hughes et al., 2019) known to 'couple well with the wind forcing' (Huthnance, 1986a). In their mode-1, they include the coastal Kelvin wave and have sea-level amplitude maximal at the coast (for low frequency – large wavelength, see Huthnance, 1986a,b; Gordon and Huthnance, 1987), quite similarly to the pattern shown in Fig. 3a. Note we found the region where sea-level changes associated with the mode are the largest (in the Irish Sea and along the Scottish coastline) is poleward of the region where the wind alignment with the local isobaths is most determinant to changes in α_1 (west of France and south of Ireland). The latter is an area where large along-coast growth in ϕ_1 is observed. Both these findings are extremely consistent with the cyclonic propagation of coastally trapped waves and the cumulative effect of the longshore wind forcing along isobath (Calafat et al., 2012; Gill and Clarke, 1974).

5. Conclusion

Wind-driven sea-level variability on the shelf can be related to circulation changes at the outer-shelf and upper-slope at subannual scales — and likely beyond, at faster and slower periodicities (Hermans et al., 2020; Chafik et al., 2019; Calafat et al., 2012; Gordon and Huthnance, 1987). The shelf sea-level variability is one of the key contributors to along-slope coherence in currents over thousands of kilometres along the European margins. Broadly speaking, a bathymetry-following, poleward (equatorward), anomalous flow can be expected to occur when elevated (depressed) sea levels relative to normal are found over the shelf. These shelf sea-level changes arise due to the convergence of Ekman currents in the presence of a sloping bathymetry and/or a coastline. Our results indicate that sea-level changes driven by Ekman transport and converted into along-isobath current through geostrophic adjustment are of prime importance for the European margin circulation.

While shelf sea-level variability generates anomalous geostrophic circulation, our results indicate these currents are limited to the upper slope and shelf. Coherent shelf sea-level changes are hence associated with a boundary circulation flowing east of the Porcupine Seabight and through the Porcupine Saddle Point rather than around the Goban Spur and the Porcupine Bank. This shallow pathway has sometimes been associated with the continuous 'European Slope Current' (Xu et al., 2015; Pingree et al., 1999), yet we recommend caution when using this term. Thus far, representations of a continuous circulation trapped at the shelf-edge and extending from Portugal (if not more to the south) to the Faroe-Shetland Channel (or more to the north) were derived from sea surface height anomalies rather than mean values (our Fig. 3b., as well as Fig. 6a. of Xu et al. 2015 or Figure 16 of Pingree et al. 1999). The mean sea surface height distribution in the region is rather different, and cannot be associated with poleward surface geostrophic flow over the slope to the south of Ireland (Diabaté et al., In Prep.). Generally speaking, the continuity of a slope circulation along European margins remains debated. Nonetheless, the poleward current locked to the eastern continental slope of the Rockall Trough (the Rockall Slope Current after Huthnance, 1986a, although it bears many other names), is influenced on its shoreward side by the anomalous flow associated with the common shelf sea-level variability.

CRediT authorship contribution statement

Sam T. Diabaté: Writing – original draft, Visualization, Software, Methodology, Investigation, Formal analysis, Data curation, Conceptualization. **Neil J. Fraser:** Writing – review & editing, Supervision, Data curation. **Martin White:** Writing – review & editing, Supervision. **Barbara Berx:** Writing – review & editing, Data curation. **Louis Marié:** Writing – review & editing, Software, Methodology, Formal analysis, Data curation. **Gerard D. McCarthy:** Writing – review & editing, Supervision, Methodology, Conceptualization.

Declaration of competing interest

The authors declare that they have no conflict of interest

Acknowledgements

This work was partly financed by the A4 Project (Aigéin, Aeráid, agus athrú Atlantaigh), with the support of the Marine Institute, under the Marine Research Programme, funded by the Irish Government Grant PBA/CC/18/01). This study was also supported by the UK Natural Environment Research Council National Capability funding (NE/R015953/1) and is a contribution to the Climate Linked Atlantic Section Science (CLASS) programme. This study was also supported by the UK Natural Environment Research Council (NERC) National Capability programme AtlantiS (NE/Y005589/1) and NERC grant ODISSEA (NE/Y005236/1).

EirOOS (the Irish Ocean Observing System) is supported in part by Science Foundation Ireland under Grant No. 18/RI/5731. Data from the LOIS-SES and OMEX programs were provided by the British Oceanographic Data Centre (BODC) and funding sources are indicated in Souza et al. (2001), Huthnance et al. (2001), White and Bowyer (1997) or references therein. Furthermore, our work makes use of data collected with the support of the Flotte Océanographique Française, during the ASPEX series of cruises (https://doi.org/10.18142/245). Moored instruments in the Faroe-Shetland Channel have been supported by the Offshore Monitoring Programme of Scottish Government's Marine Directorate and by European Framework Programmes under grant agreement No. GA212643 (THOR) and grant agreement No. 308299 (NACLIM), and from the European Union's Horizon 2020 research and innovation programme under grant agreement No. 727852 (Blue-Action), as well as the Nordic WOCE, VEINS, and MOEN projects. Finally, we use moored data obtained from http://envofar.fo/data/index.php?dir=Currents%2FADCP_Data&sort=N&order=A and Moritz et al. (2021a). Glider and moored data from the OSNAP/Ellett line can be accessed at https://thredds.sams.ac.uk/thredds/catalog/osnap.html.

Furthermore, ObsSea4Clim "Ocean observations and indicators for climate and assessments" is funded by the European Union, Horizon Europe Funding Programme for Research and Innovation under grant agreement number: 101136548. ObsSea4Clim contribution nr. 13.

Appendix A. Mooring data

A.1. Faroe–Shetland moorings

We obtained data from the bottom-mounted upward-looking ADCPs installed between Scotland and the Faroe Islands, used to monitor the Faroe-Shetland Channel transport (Berx et al., 2013; Hansen et al., 2013, 2017). These moorings are organised along three sections, which from west to east are: NWZ (Cape Wrath to South Faroe), NWS (Fair Isle to Munken) and NWE (Nolso to Muckle Flugga). The NWS line is one of the longest current monitoring array timeseries in the Northeast Atlantic. For this study, we use data from all three sections on the slope and shelf of the Scottish side. At the NWSD site, we exclude measurements collected in 2014 during the FASTNEt campaign since the mooring position was displaced more than fifteen kilometres away from its usual position. We further excluded deployments NWSD1011, NWSD0805, and NWSD0905 as we observed variance issues. The data originating from the NWSE site suffered compass issues between 2008 and 2013. These were corrected for by rotating the currents so that M2 tidal ellipse directions were consistent throughout deployments (major axis pointing ~17° anticlockwise from east). All Faroe-Shetland Channel ADCP data were provided by Dr. Barbara Berx, at the exception of currents from NWSH, which were downloaded from http://envofar.fo/data/index.php?dir=Currents%2FADCP_Data&sort=N&order=A.

A.2. OSNAP moorings

The Overturning in the Subpolar North Atlantic Program (OSNAP) is an observational mooring array which monitors the strength of the Atlantic Meridional Overturning Circulation between Scotland, Greenland, and Newfoundland. At the Rockall Trough eastern margin, two OSNAP moorings are of relevance for the present study: RT-EB1 and RT-EB0. The former is a mooring maintained since 2014 and equipped with six SPCMs sampling the whole water column. Mooring RT-EB0 (sometimes referred to as ADCP1, *e.g.* Houpert et al., 2020) was an 8-month upward-looking ADCP deployment above the 750 m isobath (approximately) in 2014–2015. Both moorings are located at ~57°N. Additionally, we use depth-averaged velocity from OSNAP glider transects in the Rockall Trough eastern wedge (Fraser et al., 2022). OSNAP moored and glider data were provided by Dr. Neil Fraser. Glider and moored data from the OSNAP/Ellett line can be accessed at https://thredds.sams.ac.uk/thredds/catalog/osnap.html.

A.3. LOIS-SES moorings

The Land Ocean Interaction Study – Shelf Edge Study (LOIS-SES) program (Souza et al., 2001; Burrows and Thorpe, 1999) operated three long-lasting moorings from Spring 1995 to Summer 1996 on the Hebridean slope, as well as several shorter deployments which are not considered here. The three rigs were located above the 140 m, 400 m, and 700 m isobath at 56°27.6N (Souza et al., 2001). The outer-shelf and shelf-edge moorings S140 and S400 were equipped with upward-looking ADCPs and functioned in a near continuous manner. The deeper mooring S700 was equipped with an array of SPCMs and measured currents during Summer 1995, and from late Winter to mid-Summer 1996, although only the period from Spring 1996 meets the depth-averaging thresholds described in Section 2. The S400 ADCP data, comprising of four deployments, notoriously suffers from compass biases (Huthnance et al., 2022). We manually re-aligned S400 data, so that the semi-major axis of the residual flow variance is, for each deployment, aligned with local isobaths (80°anticlockwise from east). The fourth and last deployment (17 days in February 1996) was found too short-lived for such editing and is not used here. The LOIS-SES historic data was retrieved from BODC.

A.4. OMEX moorings

The Ocean Margin EXchange (OMEX) program (Wollast and Chou, 2001) operated moorings on the Goban Spur and northwest of Ireland from Spring 1993 to Autumn 1995 (White and Bowyer, 1997; Huthnance et al., 2001; Pingree et al., 1999; van Aken et al., 2005). The currents were measured using SPCMs, allowing a partial depiction of the water column. Mooring PML-154 meets our depth-averaging threshold and is included in our analysis. We also use data from moorings PML-150, WBNE, and WBSW because they fill in geographical gaps (regions of little measurements). PML-150 had two SPCMs operated concurrently, but only for a four month period during the Summer 1995. For this reason, we decided to retain only the 7-month long record of the top SPCM, located approximately 30 m from the sea surface. Northwest of Ireland White and Bowyer (moorings WBNE and

WBSW, 1997), only the lowermost paddle wheel current-meters (~40 m from the seabed) were recovered from the water, and we use them here. The OMEX historic data was retrieved from the British Oceanographic Data Centre (BODC).

A.5. NOAC mooring

The NOrth Atlantic Changes (NOAC) observing array featured two instrumented moorings at its eastern boundary on the Goban Spur collecting in-situ current data since 2016 (Moritz et al., 2021b). GS-EB1 and GS-EB3 were located above the ~1530 m and ~4450 m isobaths respectively. We retrieved data from Moritz et al. (2021a, Pangaea repository). GS-EB1 was equipped with an upward-looking ADCP installed at mid-depth, and SPCMs from 750 m to the seabed. GS-EB3, equipped with SPCMs, does not meet our depth-averaging thresholds and is not used here.

A.6. ASPEX moorings

The Aquitaine/Armorican Shelves and Slopes Processes EXperiment (ASPEX) (Le Boyer et al., 2013; Kersalé et al., 2016) consisted in ten moorings on the shelf and slope of the Bay of Biscay, operated between 2009 and 2011. Moorings were equipped with bottom-mounted upward-looking ADCPs and located on three sections orientated across the shelf and slope. The northern sections (Penmarc'h and Loire) each featured three moorings above the ~60 m, ~130 m and ~450 m marks, while the 44°N section featured four moorings above the ~50 m, ~70 m, ~130 m and ~450 m isobaths. ASPEX ADCP data were contributed to the study by Dr. Louis Marié. The top 20% of ADCP bins were affected by surface reflection and removed following Le Boyer et al. (2013).

A.7. EirOOS moorings

We also include previously unpublished moored current data originating from the new EirOOS program and collected at three sites south and west of Ireland by the Marine Institute and 'A4' ocean science group at Maynooth University. The 'South Rockall Trough Mooring' (SRT) is located in ~3000 m of water off the western facade of the Porcupine Bank (15°31.2E, 52°59.9N) nearby a Met Éireann weather buoy named M6. A first deployment was conducted between October 2018 and June 2019 with two 75 kHz RDI 'Workhorse' upward-looking ADCPs installed at ~400 and ~900 m below the water surface. During this pilot leg, the bottom ADCP malfunctioned. Between May 2020 and June 2021, a second deployment with similar configuration was carried out. A third leg was conducted between April 2022 and May 2023, with the line fitted with an upward-looking Nortek Signature 55 kHz ADCP installed at a depth of approximately a thousand metres. Measurements at SRT are at present continued.

EBS5 (09°28.2E, 51°18.0N), a mooring located at proximity of the Fastnet Rock off the southern Irish coast in approximately 90 m of water, is in continued operation since June 2020. It is equipped with a RDI 300 kHz 'Workhorse' upward-looking ADCP installed within a trawl resistant bottom mount. Here we used data from the first deployment leg, from June 2020 to October 2021. During this time, the ADCP pressure sensor malfunctioned and a nominal ADCP depth of 88 m is used instead in the processing.

EBS1 was a mooring located in approximately 1000 m of water depth on the Goban Spur (12°11.1E, 49°06.8N). It was equipped with a 75 kHz RDI 'Workhorse' upward-looking ADCP installed approximately 600 m below the water surface. EBS1 was operated from March 2020 and discontinued in October 2022, at the same time as the GS-EB1 and GS-EB3 of the NOAC program (Moritz et al., 2021b). It is noteworthy that EBS1 was located less than a kilometre away from the position of the PML-154 mooring operated from January 1994 to June 1995 as part of the OMEX program.

Appendix B. Empirical orthogonal function analysis

Let us define the geophysical anomaly (with respect to a climatological temporal mean) $\chi(x_1, x_2, \ldots, x_m, t)$ a field of m spatial dimensions (say, two) and a temporal dimension.[1] The variables $x_1, x_2, \ldots, x_m$ and t are the coordinates which uniquely determine position in space and time. Such field χ can be objectively decomposed into modes of variability by means of Empirical Orthogonal Function Analysis, so that $\chi(x_1, x_2, \ldots, x_m, t)$ can be formulated as

$$\chi(x_1, x_2, \ldots, x_m, t) = \sum_i \phi_i(x_1, x_2, \ldots, x_m)\alpha_i(t), \tag{B.1}$$

where the Empirical Orthogonal Vectors or Functions (EOFs) ϕ carry the spatial information and the Principal Components (PCs) α the time varying development.

Typically, it is only possible to access discrete estimates of geophysical fields, meaning all χ dimensions have a finite length ($n_1, n_2, \ldots, n_m$ for space and n_t for time). Expressed in matrix notation, the decomposition takes the form

$$\boldsymbol{\chi} = \sum_{i=1}^{n} \phi_i \alpha_i, \tag{B.2}$$

where, if $m > 1$, spatial dimensions of the variable χ are concatenated so that spatial dependence makes up a single dimension of length $n = n_1 + n_2 + \cdots + n_m$. A decomposition of the form of Eq. (B.2) is sought such that 1) $\sum_{i=1}^{k} \phi_i \cdot \alpha_i$ tends towards χ in as little modes k as possible; and 2) the principal components have zero correlation between each other. These constraints are met when solving the eigenvalue–eigenvector problem

$$\boldsymbol{C}\phi_i = \lambda_i \phi_i \tag{B.3}$$

with λ_i the i-eth eigenvalue and C the variance–covariance matrix of $\boldsymbol{\chi}$,

$$\boldsymbol{C} = \langle \boldsymbol{\chi}\boldsymbol{\chi}^T \rangle. \tag{B.4}$$

The principal components α are obtained by projecting $\boldsymbol{\chi}$ on the eigenvector basis composed by the EOFs ϕ. This is done after the EOFs ϕ are scaled so that

$$\phi_i \cdot \phi_i = \lambda_i, \tag{B.5}$$

which allows for the empirical orthogonal functions ϕ to have same physical dimension as χ and for the principal components α to have unit variance (Ambaum, 2004). In general, most of variability of χ is contained in a few leading modes $\phi_i \cdot \alpha_i$, so that EOF analysis can be used as a dimensionality reduction tool.

Appendix C. Current standard deviation ellipses

The EOF method described in Appendix B is an eigenvalue–eigenvector decomposition in the particular context of geophysics, which typically deal with fields of one to three spatial dimension(s) and a temporal dimension. In the general case, EOF decomposition is known as principal component analysis (PCA) and is not limited to spatio-temporal fields. Broadly speaking, PCA can be performed on any two-dimensional table $\boldsymbol{\chi} = \chi(\mu, \kappa)$, where different $\mu \in [1, n]$ are different variables, and different κ are different realisations (or observations) of these variables. PCA allows for the objective reformulation of $\boldsymbol{\chi} = \chi(\mu, \kappa)$ in a new coordinate basis made up of the orthogonal (hence uncorrelated) eigenvectors of the variance–covariance matrix $\boldsymbol{C}$. Note that again, this works at the conditions that all variables have zero-mean across the realisation dimension.

[1] A typical geophysical field variable has at least one and at most three spatial dimensions ($1 \leq m \leq 3$): for example, the sea surface height anomaly $\eta(x, y, t)$.

To compute the depth-averaged current standard deviation ellipses shown in Fig. 1, $\boldsymbol{\chi}$ is constructed so that

$$\boldsymbol{\chi}^T = \begin{bmatrix} \overline{u}(t) \\ \overline{v}(t) \end{bmatrix} \tag{C.1}$$

and a EOF/PC decomposition is performed, following the steps detailed in Appendix B (Eqs. (B.2) to (B.5)). The scaled eigenvectors $\boldsymbol{\phi}$ are obtained and presented as the semi-major and semi-minor axes of the ellipses in Fig. 1. Furthermore, in this simple scenario $n = 2$ (there are only two variables), meaning the principal component analysis is solely a rotation along the main direction of current variance and

$$\boldsymbol{\phi_1}\alpha_1(t) + \boldsymbol{\phi_2}\alpha_2(t) \tag{C.2}$$

exactly equals $[\overline{u}(t), \overline{v}(t)]$.

Appendix D. Principal component based multiple linear regression (PCMLR)

D.1. System response to the wind forcing

In Section 3.2, we seek the sensitivity of the shelf sea-level variability (α_1) to the action of the wind stress, and for this purpose, we model the physical system as a (linear time-invariant) response to an external forcing,

$$\alpha_1(t) = \boldsymbol{K}\boldsymbol{X}, \tag{D.1}$$

where the external forcing $\boldsymbol{X}(t)$ is a matrix composed of the zonal and meridional surface wind stress anomalies at each non-land grid point of the atmospheric reanalysis (τ^x, τ^y). $\boldsymbol{K}$ represents the (time-invariant) response of the physical system, independent of wind large-scale co-variability and solely representing the ocean physics.

If the polluting noise in $\boldsymbol{X}(t)$ is assumed to be well-behaved, *i.e.* linearly independent of the signal in $\boldsymbol{X}(t)$, Eq. (D.1) is in fact a simple multiple linear regression,

$$\alpha_1(t) = \left(\sum_{i=1}^{n} k_i x_i(t) \right) + \mathcal{O}(t), \tag{D.2}$$

with n the total number of predictors (that is, twice the number of non-land grid points, accounting for both zonal and meridional winds) and $\mathcal{O}(t)$ an independent noise. Eq. (D.1) can be solved in a least-square sense, allowing — in principle — to obtain a system response $\boldsymbol{K}$ independent of the co-variability of the explanatory variables as desired,

$$\boldsymbol{K} = \langle \alpha_1 \boldsymbol{X}^T \rangle \langle \boldsymbol{X}\boldsymbol{X}^T \rangle^{-1}. \tag{D.3}$$

where $\langle \boldsymbol{X}\boldsymbol{X}^T \rangle$ designates the covariance matrix of $\boldsymbol{X}$. In effect, because there is great co-variability in the wind stress signal at different grid points, the obtained $\boldsymbol{K}$ is largely determined by the polluting noise, which is not in the general case well-behaved. Covariances between variables in $\boldsymbol{X}$ are not perfectly known, and the obtained $\boldsymbol{K}$ is strongly affected by the inaccuracy of the $\langle \boldsymbol{X}\boldsymbol{X}^T \rangle$ estimate. In this overfitting scenario, inferring causality from $\boldsymbol{K}$ is impossible despite fitting α_1 is easily achieved. To circumnavigate this shortcoming, we opt for a change of variables based on principal component analysis (see also, Mendeş, 2009).

Performing an eigen decomposition of the explanatory variable covariance matrix ($\langle \boldsymbol{X}\boldsymbol{X}^T \rangle = \boldsymbol{\Phi}\boldsymbol{\Lambda}\boldsymbol{\Phi}^{-1}$, with $\boldsymbol{\Phi}^{-1} = \boldsymbol{\Phi}^T$) allows to write Eq. (D.3) as[2]

$$\boldsymbol{K} = \langle \alpha_1 \boldsymbol{\Gamma}^T \rangle \boldsymbol{\Phi}^T \boldsymbol{\Phi} \boldsymbol{\Lambda}^{-1} \boldsymbol{\Phi}^T, \tag{D.4}$$

where $\boldsymbol{\Gamma}$ is a matrix containing the wind stress anomalies principal components ($\boldsymbol{X} = \boldsymbol{\Phi}\boldsymbol{\Gamma} = \varphi_1(x,y)\gamma_1(t) + \cdots + \varphi_n(x,y)\gamma_n(t)$). Eqs. (D.3) and (D.4) are exactly equivalent, but the latter simplifies considerably to

$$\boldsymbol{Q} = \boldsymbol{K}\boldsymbol{\Phi} = \langle \alpha_1 \boldsymbol{\Gamma}^T \rangle \boldsymbol{\Lambda}^{-1}, \tag{D.5}$$

which is a multiple linear regression onto the principal components of the wind stress anomalies:

$$\alpha_1(t) = \left(\sum_{i=1}^{n} q_i \gamma_i(t) \right) + \mathcal{O}(t). \tag{D.6}$$

The sensitivity of α_1 to the wind variability is hence sought by solving the multiple linear regression of Eq. (D.6) to obtain $\boldsymbol{Q}$. Exclusion or inclusion in the regression of each of the principal components γ_i is objectively determined using the adjusted coefficient of determination R^2,

$$R^2 = 1 - \frac{\sum_{i=1}^{n_t} (\alpha_1 - \boldsymbol{Q}_T \boldsymbol{\Gamma}_T)^2 (n_t - p)^{-1}}{\sum_{i=1}^{n_t} \alpha_1^2 (n_t - 1)^{-1}}, \tag{D.7}$$

with $\boldsymbol{\Gamma}_T$ the matrix of explanatory principal components truncated of $m = n - p$ modes and n_t is the total number of temporal points. The system response $\boldsymbol{K}$ is then obtained by projecting $\boldsymbol{Q}_T$ onto the truncated eigenvector basis $\boldsymbol{\Phi}_T$ (Eq. (D.5)). The method has the intrinsic interest that it does not leave 'holes' in the map of $\boldsymbol{K}$. Rather than having to remove grid points, higher eigen modes are removed.

We compute the sums in Eq. (D.7) over the total number of temporal points (365 days×29 years = 10585 days), but estimate n_t in the bracket terms by dividing this value by the low-pass cut-off period (20 days); this gives a value of $n_t \approx 530$. A 'leave-one-out' procedure is then used to maximise R^2 (we do not test all possible combinations, but simply determine whether adding more principal components improve the R^2 or not), and we determine the best model includes the first $p = 81$ eigenvalues–eigenvectors.

D.2. Significance test

To test for the significance of the obtained patterns, we model $\boldsymbol{K}$ at each and every grid point as a bivariate normal distribution with zero mean and unknown covariances ($\boldsymbol{K}_{ij} \sim \mathcal{N}(\boldsymbol{\mu_0} = \boldsymbol{0}, \boldsymbol{\Sigma}_{ij})$, where ij indicates the grid point). The rationale behind the choice to model $\boldsymbol{K}_{ij} = (K^x, K^y)$ as a normal distribution is that 1. the shelf mode principal component α_1 is approximately normally distributed (Fig. 4 c); 2. $\boldsymbol{K}_{ij}$ is obtained through linear combination of the α_1 elements (Eq. (D.4)); and 3. a linear transformation of a normal distribution is also normal.

For readability, we will drop the notation $_{ij}$. The probability that $\boldsymbol{K} = (K^x, K^y)$ takes (X, Y) for values is

$$P(X,Y) = \frac{1}{2\pi\sqrt{|\boldsymbol{\Sigma}|}} \exp\left(-\frac{\boldsymbol{X}^T \boldsymbol{\Sigma}^{-1} \boldsymbol{X}}{2} \right), \tag{D.8}$$

where $\boldsymbol{\Sigma} = \boldsymbol{K}\boldsymbol{K}^T$ is the variance–covariance matrix of $\boldsymbol{K}$, $|\boldsymbol{\Sigma}|$ the associated determinant and $\boldsymbol{X}^T = [X, Y]$. It is helpful to diagonalise $\boldsymbol{\Sigma}$ so that $\boldsymbol{\Sigma} = \boldsymbol{B}\boldsymbol{\Lambda}\boldsymbol{B}^T$, where $\boldsymbol{B}$ is made up of the eigenvectors $\boldsymbol{B_1}$ and $\boldsymbol{B_2}$ and $\boldsymbol{\Lambda}$ is composed of the associated eigenvalues λ_1 and λ_2.[3]

The probability Q that a random sample lies inside the ellipse of equi-probability $P = P(X,Y)$ is

$$Q = 1 - \exp\left(-\frac{(\boldsymbol{B_1} \cdot \boldsymbol{X})^2}{2\lambda_1} - \frac{(\boldsymbol{B_2} \cdot \boldsymbol{X})^2}{2\lambda_2} \right). \tag{D.9}$$

Swapping $\boldsymbol{X}$ for the true sensitivity $\boldsymbol{K}$ in Eq. (D.9) allows to obtain the significance of $\boldsymbol{K}$ provided $\boldsymbol{B}$ and $\boldsymbol{\Lambda}$ are estimated. For this

[2] The eigenvalue decomposition here described is exactly similar to the EOF method for geophysical variables described in Appendix B.

[3] The eigenvalue–eigenvector decomposition here described is akin to the EOF method for vectors described in Appendix C.

purpose, $M = 1000$ surrogates of the principal component α_1 were generated retaining its Fourier transform magnitude but randomising its phase (similarly to Ebisuzaki, 1997). These random timeseries were then used to generate M sensitivity maps, following M-times the PCMLR method (note that for consistency the number p of wind stress modes considered is kept unchanged at 81). The matrices $\mathcal{B}$ and Λ are estimated at each map grid points from the surrogate-obtained distribution, and significance is obtained.

Appendix E. Seasonal modulation of the 20–360 day bandpass-filtered sea-level variance

The variance of the 20–360 day bandpass-filtered sea surface height is generally greater in winter that in summer (not shown), in part because the atmospheric forcing itself features seasonal changes in variance, but also for other reasons (seasonal variations in stratification at the slope can also affect the system response — in particular, they can change coastally trapped wave characteristics, see Hughes et al., 2019; Mysak, 1980). EOF decomposition assumes temporal stationarity in the covariance between sea surface height observations at different gridpoints. Here, this signifies that the principal components α carry *all* of the seasonal cycle in the sea-level variance, while the empirical orthogonal functions ϕ do not carry any. Involved techniques exist to circumvent this shortcoming (Kim and Wu, 1999; Kim et al., 2015, 2018), effectively rendering ϕ periodically time-dependent. In the present case, this limitation is not a major issue as the seasonal cycle in the variance is much smaller than the total variance. We simply note that α_1 tends to take extremum values (positives or negatives) more often in winter than in summer, and do not attempt to quantify how these changes affect the return-period statistics or the links with the atmospheric variability and in-situ currents.

References

van Aken, H.M., Maas, L.R., van Haren, H., 2005. Observations of inertial wave events near the continental slope off Goban Spur. J. Phys. Oceanogr. 35 (8), 1329–1340. http://dx.doi.org/10.1175/JPO2769.1.

Ambaum, M.H.P., 2004. Calculating EOFs and principal component time-series.

Ballarotta, M., Ubelmann, C., Pujol, M.-I., Taburet, G., Fournier, F., Legeais, J.-F., Faugère, Y., Delepoulle, A., Chelton, D., Dibarboure, G., Picot, N., 2019. On the resolutions of ocean altimetry maps. Ocean. Sci. 15 (4), 1091–1109. http://dx.doi.org/10.5194/os-15-1091-2019.

Berx, B., Hansen, B., Østerhus, S., Larsen, K.M., Sherwin, T., Jochumsen, K., 2013. Combining in situ measurements and altimetry to estimate volume, heat and salt transport variability through the Faroe–Shetland channel. Ocean. Sci. 9 (4), 639–654. http://dx.doi.org/10.5194/os-9-639-2013.

Burrows, M., Thorpe, S., 1999. Drifter observations of the Hebrides slope current and nearby circulation patterns. In: Annales Geophysicae. vol. 17, no. 2, Springer Verlag Göttingen, Germany, pp. 280–302. http://dx.doi.org/10.1007/s00585-999-0280-5.

Calafat, F.M., Chambers, D.P., Tsimplis, M.N., 2012. Mechanisms of decadal sea level variability in the eastern North Atlantic and the Mediterranean Sea. J. Geophys. Res.: Ocean. 117 (C9), http://dx.doi.org/10.1029/2012JC008285.

Chafik, L., Nilsen, J.E.Ø., Dangendorf, S., 2017. Impact of North Atlantic teleconnection patterns on Northern European sea level. J. Mar. Sci. Eng. 5 (3), 43. http://dx.doi.org/10.3390/jmse5030043.

Chafik, L., Nilsen, J.E.Ø., Dangendorf, S., Reverdin, G., Frederikse, T., 2019. North Atlantic Ocean circulation and decadal sea level change during the altimetry era. Sci. Rep. 9 (1), 1041. http://dx.doi.org/10.1038/s41598-018-37603-6.

Diabaté, S.T., Fraser, N.J., White, M., McCarthy, G.D., On the discontinuity of the European Slope Current (in preparation).

Ebisuzaki, W., 1997. A method to estimate the statistical significance of a correlation when the data are serially correlated. J. Clim. 10 (9), 2147–2153. http://dx.doi.org/10.1175/1520-0442(1997)010<2147:AMTETS>2.0.CO;2.

Fraser, N.J., Cunningham, S.A., Drysdale, L.A., Inall, M.E., Johnson, C., Jones, S.C., Burmeister, K., Fox, A.D., Dumont, E., Porter, M., Holliday, N.P., 2022. North Atlantic Current and European slope current circulation in the Rockall Trough observed using moorings and gliders. J. Geophys. Res.: Ocean. e2022JC019291. http://dx.doi.org/10.1029/2022JC019291.

Gill, A.E., Clarke, A.J., 1974. Wind-induced upwelling, coastal currents and sea-level changes. Deep-Sea Res. Ocean. Abstr. 21 (5), 325–345. http://dx.doi.org/10.1016/0011-7471(74)90038-2.

Gordon, R.L., Huthnance, J.M., 1987. Storm-driven continental shelf waves over the scottish continental shelf. Cont. Shelf Res. 7 (9), 1015–1048. http://dx.doi.org/10.1016/0278-4343(87)90097-5.

Hansen, B., Larsen, K.M., Hátún, H., Kristiansen, R., Mortensen, E., Berx, B., Sherwin, T., Østerhus, S., Quadfasel, D., Jochumsen, K., 2013. Monitoring the Flow of Atlantic Water Through the Faroe–Shetland Channel. Technical Report, Havstovan Technical Report, 13–13, 22 p., available at: http://www.hav.fo/wp-content/uploads/2024/04/TecRep1313.pdf.

Hansen, B., Poulsen, T., Húsgarð Larsen, K.M., Hátún, H., Østerhus, S., Darelius, E., Berx, B., Quadfasel, D., Jochumsen, K., 2017. Atlantic water flow through the faroese channels. Ocean. Sci. 13 (6), 873–888. http://dx.doi.org/10.5194/os-13-873-2017.

Hermans, T.H.J., Le Bars, D., Katsman, C.A., Camargo, C.M.L., Gerkema, T., Calafat, F.M., Tinker, J., Slangen, A.B.A., 2020. Drivers of interannual sea level variability on the Northwestern European shelf. J. Geophys. Res.: Ocean. 125 (10), e2020JC016325. http://dx.doi.org/10.1029/2020JC016325.

Hogarth, P., Hughes, C., Williams, S., Wilson, C., 2020. Improved and extended tide gauge records for the British Isles leading to more consistent estimates of sea level rise and acceleration since 1958. Prog. Oceanogr. 184, 102333. http://dx.doi.org/10.1016/j.pocean.2020.102333.

Holgate, S.J., Matthews, A., Woodworth, P.L., Rickards, L.J., Tamisiea, M.E., Bradshaw, E., Foden, P.R., Gordon, K.M., Jevrejeva, S., Pugh, J., 2013. New data systems and products at the permanent service for mean sea level. J. Coast. Res. 29 (3), 493–504. http://dx.doi.org/10.2112/JCOASTRES-D-12-00175.1.

Houpert, L., Cunningham, S., Fraser, N., Johnson, C., Holliday, N.P., Jones, S., Moat, B., Rayner, D., 2020. Observed variability of the North Atlantic Current in the Rockall Trough from 4 years of mooring measurements. J. Geophys. Res.: Ocean. 125 (10), e2020JC016403. http://dx.doi.org/10.1029/2020JC016403.

Hughes, C.W., Fukumori, I., Griffies, S.M., Huthnance, J.M., Minobe, S., Spence, P., Thompson, K.R., Wise, A., 2019. Sea level and the role of coastal trapped waves in mediating the influence of the open ocean on the coast. Surv. Geophys. 40, 1467–1492. http://dx.doi.org/10.1007/s10712-019-09535-x.

Huthnance, J.M., 1986a. The Rockall slope current and shelf-edge processes. Proc. R. Soc. Edinb. Sect. B: Biol. Sci. 88, 83–101. http://dx.doi.org/10.1017/S0269727000004486.

Huthnance, J., 1986b. The subtidal behaviour of the Celtic Sea—III. A model of shelf waves and surges on a wide shelf. Cont. Shelf Res. 5 (3), 347–377. http://dx.doi.org/10.1016/0278-4343(86)90003-8.

Huthnance, J.M., Coelho, H., Griffiths, C.R., Knight, P.J., Rees, A.P., Sinha, B., Vangriesheim, A., White, M., Chatwin, P.G., 2001. Physical structures, advection and mixing in the region of Goban spur. Deep. Sea Res. Part II: Top. Stud. Ocean. 48 (14–15), 2979–3021. http://dx.doi.org/10.1016/S0967-0645(01)00030-3.

Huthnance, J.M., Hopkins, J., Berx, B., Dale, A., Holt, J., Hosegood, P., Inall, M., Jones, S., Loveday, B.R., Miller, P.I., Polton, J., Porter, M., Spingys, C., 2022. Ocean shelf exchange, NW European shelf seas: Measurements, estimates and comparisons. Prog. Oceanogr. 202, 102760. http://dx.doi.org/10.1016/j.pocean.2022.102760.

Kanamitsu, M., Ebisuzaki, W., Woollen, J., Yang, S.K., Hnilo, J.J., Fiorino, M., Potter, G.L., 2002. NCEP–DOE AMIP-II Reanalysis (R-2). Bull. Am. Meteorol. Soc. 83 (11), 1631–1644. http://dx.doi.org/10.1175/BAMS-83-11-1631.

Kersalé, M., Marie, L., Le Cann, B., Serpette, A., Lathuilière, C., Le Boyer, A., Rubio, A., Lazure, P., 2016. Poleward along-shore current pulses on the inner shelf of the bay of biscay. Estuar. Coast. Shelf Sci. 179, 155–171. http://dx.doi.org/10.1016/j.ecss.2015.11.018.

Kim, K.Y., Hamlington, B., Na, H., 2015. Theoretical foundation of cyclostationary EOF analysis for geophysical and climatic variables: concepts and examples. Earth-Sci. Rev. 150, 201–218. http://dx.doi.org/10.1016/j.earscirev.2015.06.003.

Kim, K.Y., Lim, C.Y., Kim, E.J., 2018. A new approach to the space–time analysis of big data: application to subway traffic data in seoul. J. Big Data 5 (1), 5. http://dx.doi.org/10.1186/s40537-018-0116-9.

Kim, K.-Y., Wu, Q., 1999. A comparison study of EOF techniques: Analysis of nonstationary data with periodic statistics. J. Clim. 12 (1), 185–199. http://dx.doi.org/10.1175/1520-0442(1999)012<0185:ACSOET>2.0.CO;2.

Le Boyer, A., Charria, G., Le Cann, B., Lazure, P., Marié, L., 2013. Circulation on the shelf and the upper slope of the Bay of Biscay. Cont. Shelf Res. 55, 97–107. http://dx.doi.org/10.1016/j.csr.2013.01.006.

Mendeş, M., 2009. Multiple linear regression models based on principal component scores to predict slaughter weight of broiler. Arch. Geflugelkd. 73 (2), 139–144. http://dx.doi.org/10.1016/S0003-9098(25)00852-5.

Moat, B., Burmeister, K., Firing, Y., 2022. CLASS and OSNAP Report for JC238. Technical Report, National Oceanography Centre, URL: https://nora.nerc.ac.uk/id/eprint/533744/1/JC238_cruise_report_final.pdf.

Monahan, A.H., Fyfe, J.C., Ambaum, M.H., Stephenson, D.B., North, G.R., 2009. Empirical orthogonal functions: The medium is the message. J. Clim. 22 (24), 6501–6514. http://dx.doi.org/10.1175/2009JCLI3062.1.

Moritz, M., Jochumsen, K., Kieke, D., Klein, B., Klein, H., Köllner, M., Rhein, M., 2021a. Current meter measurement data and volume transport time series from deep-sea moorings deployed in the North Atlantic Eastern Boundary (EB) region at Goban Spur. http://dx.doi.org/10.1594/PANGAEA.932566.

Moritz, M., Jochumsen, K., Kieke, D., Klein, B., Klein, H., Köllner, M., Rhein, M., 2021b. Volume transport time series and variability of the North Atlantic eastern boundary current at Goban Spur. J. Geophys. Res.: Ocean. 126 (9), e2021JC017393. http://dx.doi.org/10.1029/2021JC017393.

Mysak, L.A., 1980. Topographically trapped waves. Annu. Rev. Fluid Mech. 12 (1), 45–76. http://dx.doi.org/10.1146/annurev.fl.12.010180.000401.

Permanent Service for Mean Sea Level, 2023. Tide gauge dataset. URL: http://www.psmsl.org/data/obtaining/.

Pingree, R., Le Cann, B., 1989. Celtic and armorican slope and shelf residual currents. Prog. Oceanogr. 23 (4), 303–338. http://dx.doi.org/10.1016/0079-6611(89)90003-7.

Pingree, R., Sinha, B., Griffiths, C., 1999. Seasonality of the European slope current (Goban Spur) and ocean margin exchange. Cont. Shelf Res. 19 (7), 929–975. http://dx.doi.org/10.1016/S0278-4343(98)00116-2.

Plag, H.-P., Tsimplis, M., 1999. Temporal variability of the seasonal sea-level cycle in the North Sea and Baltic Sea in relation to climate variability. Glob. Planet. Change 20 (2), 173–203. http://dx.doi.org/10.1016/S0921-8181(98)00069-1.

Pujol, M.I., Taburet, G., SL-TAC team, 2023. QUID for sea level TAC DUACS products. URL: https://catalogue.marine.copernicus.eu/documents/QUID/CMEMS-SL-QUID-008-032-068.pdf. (Accessed 01 August 2023).

Souza, A.J., Simpson, J.H., Harikrishnan, M., Malarkey, J., 2001. Flow structure and seasonality in the Hebridean slope current. Oceanol. Acta 24, 63–76. http://dx.doi.org/10.1016/S0399-1784(00)01103-8.

White, M., Bowyer, P., 1997. The shelf-edge current north-west of Ireland. In: Annales Geophysicae. vol. 15, no. 8, Springer, pp. 1076–1083. http://dx.doi.org/10.1007/s00585-997-1076-0.

Wollast, R., Chou, L., 2001. Ocean margin exchange in the Northern Gulf of Biscay: OMEX I. An introduction. Deep. Sea Res. Part II: Top. Stud. Ocean. 48 (14–15), 2971–2978. http://dx.doi.org/10.1016/S0967-0645(01)00029-7.

Xu, W., Miller, P.I., Quartly, G.D., Pingree, R.D., 2015. Seasonality and interannual variability of the European Slope Current from 20 years of altimeter data compared with in situ measurements. Remote Sens. Environ. 162, 196–207. http://dx.doi.org/10.1016/j.rse.2015.02.008.